JOURNAL OF GEOPHYSICAL RESEARCH: OCEANS, VOL. 118, 5686–5702, doi:10.1002/jgrc.20406, 2013

Absolute and convective instabilities and their roles in the forecasting of large frontal meanderings

X. San Liang[1,2,3] and Allan R. Robinson[2,4]

Received 13 May 2013; revised 23 August 2013; accepted 19 September 2013; published 22 October 2013.

[1] Frontal meanderings are generally difficult to predict. In this study, we demonstrate through an exercise with the Iceland-Faeroe Front (IFF) that satisfactory predictions may be achieved with the aid of hydrodynamic instability analysis. As discovered earlier on, underlying the IFF meandering is a convective instability in the western boundary region followed by an absolute instability in the interior; correspondingly the disturbance growth reveals a switch of pattern from spatial amplification to temporal amplification. To successfully forecast the meandering, the two instability processes must be faithfully reproduced. This sets stringent constraints for the tunable model parameters, e.g., boundary relaxation, temporal relaxation, eddy diffusivity, etc. By analyzing the instability dispersion properties, these parameters can be rather accurately set and their respective ranges of sensitivity estimated. It is shown that too much relaxation inhibits the front from varying; on the other hand, too little relaxation may have the model completely skip the spatial growth phase, leading to a meandering way more upstream along the front. Generally speaking, dissipation/diffusion tends to stabilize the simulation, but unrealistically large dissipation/diffusion could trigger a spurious absolute instability, and hence a premature meandering intrusion. The belief that taking in more data will improve the forecast does not need to be true; it depends on whether the model setup admits the two instabilities. This study may help relieve modelers from the laborious and tedious work of parameter tuning; it also provides us criteria to distinguish a physically relevant forecast from numerical artifacts.

Citation: Liang, X. S., and A. R. Robinson (2013), Absolute and convective instabilities and their roles in the forecasting of large frontal meanderings, *J. Geophys. Res. Oceans*, *118*, 5686–5702, doi:10.1002/jgrc.20406.

1. Introduction

[2] Fronts are ubiquitous in the ocean, and frontal variabilities, usually in the form of large meanderings, are an important part of oceanic variabilities. Frontal meanderings are in nature highly nonlinear and hence generally difficult to predict, especially when one seeks quantitative accuracy rather than qualitative agreement in a statistical sense. In this case one needs to take into account, for example, the agreement in geometry, location, timing, etc.

[3] Let us assume that our models are sophisticated enough to capture all the physics of frontal variation. The question to ask is: how should a model be set up to achieve a faithful simulation? A model setup includes model configuration, parameter setting, data assimilation, etc. In numerical modeling, perhaps the most tedious and laborious part of work is parameter tuning, as usually the parameters can only be empirically set. This especially becomes a problem in the tuning of those engineering parameters, such as boundary and temporal relaxations, which are not part of the underlying physics, but simply manipulations to ensure numerical stability or consistency. Which set of parameters should we choose? Why should one particular set be preferred to another? These issues must be carefully addressed before a reliable simulation, particularly a simulation without a priori knowledge of the future, can be made.

[4] Fundamentally, what we need from a simulation is, first of all, a correct reproduction of the dynamical processes. It is meaningless (and precarious) just emphasizing numerical accuracy while overlooking physical correctness. Our answer to the above questions is, accordingly, *model setup must admit the dynamical processes underlying the targeting phenomenon, and parameter tuning should not hurt these processes*. This is the rule of thumb in guiding the setup of a model. In the case of frontal meanderings, it has been observed that the underlying process often appears in the form of a convective instability followed by an absolute instability, and hence a spatial amplification locked into a

[1]School of Marine Sciences, Nanjing University of Information Science and Technology (Nanjing Institute of Meteorology), Nanjing, China.
[2]School of Engineering and Applied Sciences, Harvard University, Cambridge, Massachusetts, USA.
[3]China Institute for Advanced Study, Central University of Finance and Economics, Beijing, China.
[4]Department of Earth and Planetary Sciences, Harvard University, Cambridge, Massachusetts, USA.

Corresponding author: X. S. Liang, School of Marine Sciences, Nanjing University of Information Science and Technology (Nanjing Institute of Meteorology), 219 Ningliu Blvd., Nanjing 210044, China. (sanliang@courant.nyu.edu)

2169-9275/13/10.1002/jgrc.20406

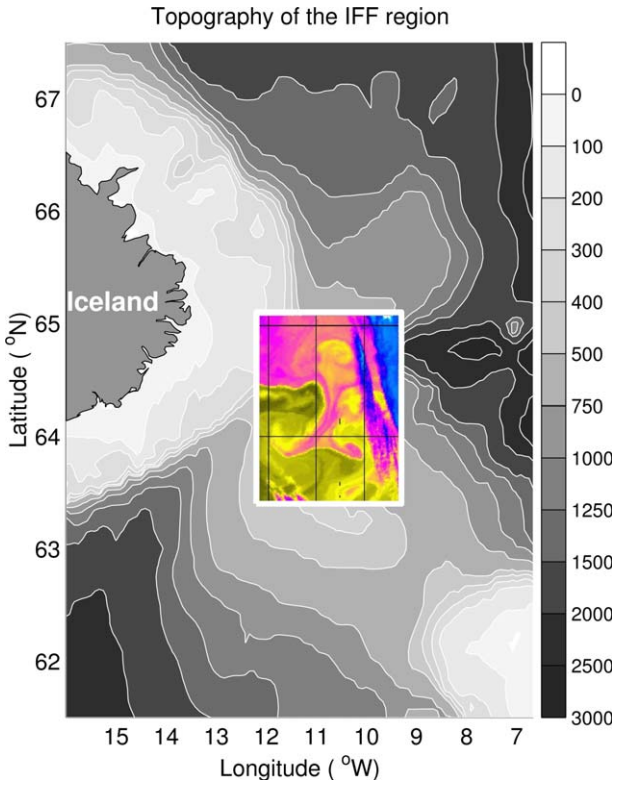

Figure 1. Topography of the Iceland-Faeroe front region (depth in meters). Boxed on the map is the IFF93 experiment domain. It is overlapped with a satellite image of the surface temperature on 22 August 1993, which displays a clear deep-sock or hammer-head meandering.

temporally growing mode. To successfully forecast this type of strong growth events, one thus must have the model set up so that the process is not suppressed or altered. Other strategies, such as taking in more observations, are by comparison only of secondary importance.

[5] We demonstrate this with a real ocean front, namely, the Iceland-Faeroe front or IFF for short. The IFF is a narrow band with sharp gradients of temperature and salinity separating the Arctic waters from the North Atlantic waters (Figure 1). Its importance in climate study, fishery industry, military operation, as well as physical oceanography, has been well documented in the literature; refer to *Meincke* [1978], *Muller et al.* [1979], *Smart* [1984], *Gould et al.* [1987], *Scott and Lane* [1990], *Hopkins* [1991], *Niiler et al*. [1992], *Read and Pollad* [1992], *Pistek and Johnson* [1992], *Allen et al*. [1994], *Miller et al*. [1996], *Hansen and Osterhusb* [2000], *Kostianoy et al*. [2004], *Astporsson et al*. [2007], and the references therein. We choose the IFF for our demonstration for two reasons. First, the available high-quality observations make this region an ideal test bed. In August 1993, an unprecedented data set (IFF93 hereafter) was acquired from the cruise of R/V *Alliance* by Harvard University in collaboration with SACLANT Undersea Center [*Robinson et al*., 1996]. It is composed of data from three surveys intended for, respectively, model initialization, enhanced adaptive observation, and model validation. Particularly, a matured meandering intrusion was captured during the third survey, providing a very nice data set for validation. Second, the intrinsic high variability of the IFF, both in space and in time, makes the IFF forecast a touchstone for the aforementioned parameter tuning rule. So far there have been several numerical studies on this front, e.g., *Miller et al*. [1995a, 1995b], *Griffiths* [1995], *Fox and Maskell* [1996], *Robinson et al*. [1996], and *Miller and Cornuelle* [1999], to name several. But how to simulate it well remains a challenge. We have, after more than 150 experiments with different combinations of parameters [see *Liang and Robinson*, 2004], eventually obtained a successful simulation of the observed meandering intrusion in terms of geometry, location, and timing. This success, however, is based on the availability of the intrusion observation; if it were a forecast without knowledge of the future, one would have no idea which to pick among the different predictions. As will be seen later, the common practice to update with more data does not necessarily lead to a better result. In this study, we will use our "rule of thumb"—parameter tuning should not hurt the underlying process(es)—as a constraint to achieve the goal of simulation/prediction. Particularly, we hope to apply this rule to select out a definite set of parameters to reduce the effort of repetitive experiments. Here we do not claim that we can completely solve the problem of parameter tuning, but only show that we have a successful try that may be enlightening, and may help relieve modelers from the laborious and tedious work. Our objectives are, to be specific, (1) among the many tunable parameters, find the most critical one(s); (2) for the critical parameter(s), find the definition interval on which the model dynamics is relevant.

[6] For the IFF meandering, it has been discovered by *Liang and Robinson* [2004] that the underlying dynamical process is a convective instability in the western boundary region followed by an absolute instability in the interior, and hence a spatial amplification locked into a temporally growing mode. The admissibility of the two instabilities, together with the allowance of an appropriate timing and order of occurrence, forms constraints in configuring the model. We therefore expect that an adequate set of parameters can be chosen through stability analysis. Indeed, as one will see soon, the formidable parameter tuning process can be greatly reduced by studying the dispersion properties of the convective and absolute instabilities. In the following, the instability model is first introduced, and then analyzed to identify the tunable parameters that may affect significantly the forecast. This model is put to application with the IFF93 data set. In section 3, the data are briefly described (section 3.1); and substituted for the background fields in the instability model (section 3.2) to yield the dispersion relation and other instability properties as needed (section 3.3). A definite set of parameters for the forecast is accordingly determined; also determined are the respective definition intervals of these parameters. The forecast is reported in section 4; it is followed by a section of sensitivity studies (section 5). These two sections serve to verify the analytical results of section 3. As an aside, section 6 investigates the effect of taking in extra observational data. This study is closed in section 7 with a brief conclusive discussion of the issues that have been raised.

2. The Instability Model

[7] We will be using the Harvard Ocean Prediction System (HOPS) to illustrate the analysis and fulfill the forecast.

To ensure the well-posedness of the problem and stabilize the integration, the HOPS applies a Newtonian nudging on each horizontal open boundary (see Appendix A and *Lozano et al*. [1994]). The boundary conditions are thence not felt by the interior points immediately. They are relaxed to the interior values within a spatial distance and a time period. This boundary nudging reduces possible mismatches in the conditions that are specified and then a longer integration may be attained. We hence consider the primitive equations with Newtonian damping:

$$\frac{\partial \rho}{\partial t}+u\frac{\partial \rho}{\partial x}+v\frac{\partial \rho}{\partial y}+w\frac{\partial \rho}{\partial z}=\nu_T\frac{\partial^2 \rho}{\partial z^2}+K_T\nabla^2\rho-C_T(\rho-\overline{\rho}), \quad (1)$$

$$\frac{\partial u}{\partial t}+u\frac{\partial u}{\partial x}+v\frac{\partial u}{\partial y}+w\frac{\partial u}{\partial z}-fv=-\frac{1}{\rho_0}\frac{\partial P}{\partial x}+\nu_M\frac{\partial^2 u}{\partial z^2}+K_M\nabla^2 u-C_M(u-\overline{u}), \quad (2)$$

$$\frac{\partial v}{\partial t}+u\frac{\partial v}{\partial x}+v\frac{\partial v}{\partial y}+w\frac{\partial v}{\partial z}+fu=-\frac{1}{\rho_0}\frac{\partial P}{\partial y}+\nu_M\frac{\partial^2 v}{\partial z^2}+K_M\nabla^2 v-C_M(v-\overline{v}), \quad (3)$$

$$\frac{\partial P}{\partial z}=-\rho g, \quad (4)$$

$$\frac{\partial u}{\partial x}+\frac{\partial v}{\partial y}+\frac{\partial w}{\partial z}=0, \quad (5)$$

where ∇^2 is the horizontal Laplacian, and the subscripts T and M for the eddy viscosity/diffusivity stand for "tracer" and "momentum," respectively. We are interested in the growth from some equilibrium or mean state $(\overline{u},\overline{v},\overline{\rho})$, which is supposed to depend on (y, z) only (based on the observation, usually $(\overline{v},\overline{w})/\overline{u}\ll O(1)$ when a west-east aligning front is studied)

$$(\overline{u},\overline{v},\overline{\rho})=(\overline{u},\overline{v},\overline{\rho})(y,z).$$

(Note we are just studying for a certain section the possibility of instability and its corresponding stability structure, not for the whole IFF configuration; in reality, the IFF need not be zonally straight, and the C in the HOPS varies with x, too.) The mean state variables are usually extracted from a simulation. The pressure can be found by integrating the hydrostatic equation:

$$P=P_{bottom}+\int_{-H}^{z}(-\rho g)\mathrm{d}z.$$

In many problems the bottom pressure P_{bottom} may be taken as spatially invariant. This is actually what is done in a reduced gravity model, where the infinite deep layer has a constant pressure: with a finite flux, the infinite depth implies a zero flow, and by geostrophy the pressure gradient must vanish. If, furthermore, the bottom is flat, we have

$$\nabla P=-g\int_{-H}^{z}\nabla\rho\mathrm{d}z. \quad (6)$$

Of course the IFF region does not have a flat bottom. But our purpose here is just for parameter estimation and, as we will see soon, this approximation is good enough for the frontal configuration.

[8] Now perturb the system from the mean state:

$$\begin{aligned}\rho&=\overline{\rho}+\rho',\\ u&=\overline{u}+u',\\ v&=\overline{v}+v',\\ w&=\overline{w}+w'.\end{aligned}$$

Linearizing, and observing that usually $(\overline{v},\overline{w})/\overline{u}\ll O(1)$ when a west-east aligning front is studied, we get

$$\frac{\partial \rho'}{\partial t}+\overline{u}\frac{\partial \rho'}{\partial x}+v'\frac{\partial \overline{\rho}}{\partial y}+w'\frac{\partial \overline{\rho}}{\partial z}=\nu_T\frac{\partial^2 \rho'}{\partial z^2}+K_T\nabla^2\rho'-C_T\rho', \quad (7)$$

$$\frac{\partial u'}{\partial t}+\overline{u}\frac{\partial u'}{\partial x}+v'\frac{\partial \overline{u}}{\partial y}+w'\frac{\partial \overline{u}}{\partial z}-fv'=\frac{g}{\rho_0}\int_{-H}^{z}\frac{\partial \rho'}{\partial x}\mathrm{d}z+\nu_M\frac{\partial^2 u'}{\partial z^2}+K_M\nabla^2u'-C_Mu', \quad (8)$$

$$\frac{\partial v'}{\partial t}+\overline{u}\frac{\partial v'}{\partial x}+fu'=\frac{g}{\rho_0}\int_{-H}^{z}\frac{\partial \rho'}{\partial y}\mathrm{d}z+\nu_M\frac{\partial^2 v'}{\partial z^2}+K_M\nabla^2v'-C_Mv', \quad (9)$$

$$\frac{\partial u'}{\partial x}+\frac{\partial v'}{\partial y}+\frac{\partial w'}{\partial z}=0. \quad (10)$$

The diagnostic variable w can be obtained from the continuity equation, using the rigid-lid assumption (an assumption adopted in the HOPS):

$$w'=-\int_0^z\left(\frac{\partial u'}{\partial x}+\frac{\partial v'}{\partial y}\right)\mathrm{d}z. \quad (11)$$

[9] Considering a solution of the form

$$\left(u',v',\rho'\right)=\left(A_u(y,z),A_v(y,z),A_\rho(y,z)\right)e^{i(\omega t-kx)}, \quad (12)$$

the above equations result in

$$\begin{aligned}&\left(i\omega+k^2K_M+C_M\right)A_u=ik\overline{u}A_u-\left(\frac{\partial \overline{u}}{\partial y}-f\right)A_v\\&-\frac{\partial \overline{u}}{\partial z}\int_0^z\left(ikA_u-\frac{\partial A_v}{\partial y}\right)\mathrm{d}z+K_M\frac{\partial^2 A_u}{\partial y^2}+\nu_M\frac{\partial^2 A_u}{\partial z^2}\\&-ik\frac{g}{\rho_0}\int_{-H}^{z}A_\rho\mathrm{d}z,\end{aligned} \quad (13)$$

$$\begin{aligned}&\left(i\omega+k^2K_M+C_M\right)A_v=-fA_u+ik\overline{u}A_v+K_M\frac{\partial^2 A_v}{\partial y^2}\\&+\nu_M\frac{\partial^2 A_v}{\partial z^2}+\frac{g}{\rho_0}\int_{-H}^{z}\frac{\partial A_\rho}{\partial y}\mathrm{d}z,\end{aligned} \quad (14)$$

$$\begin{aligned}\left(i\omega+k^2K_T+C_T\right)A_\rho=&-\frac{\partial \overline{\rho}}{\partial y}A_v-\frac{\partial \overline{\rho}}{\partial z}\int_0^z\left(ikA_u-\frac{\partial A_v}{\partial y}\right)\mathrm{d}z\\&+ik\overline{u}A_\rho+K_T\frac{\partial^2 A_\rho}{\partial y^2}+\nu_T\frac{\partial^2 A_\rho}{\partial z^2}.\end{aligned} \quad (15)$$

These equations together with, for the time being, the simple zero-gradient conditions for both vertical and horizontal boundaries:

$$\frac{\partial A_u}{\partial z}, \frac{\partial A_v}{\partial z}, \frac{\partial A_\rho}{\partial z} = 0 \qquad \text{at } z = 0, -H \tag{16}$$

$$\frac{\partial A_u}{\partial y}, \frac{\partial A_v}{\partial y}, \frac{\partial A_\rho}{\partial y} = 0 \qquad \text{at } y \text{ boundaries} \tag{17}$$

(equivalent to no heat and salinity fluxes across the surface and bottom, and no wind forcing and no bottom friction) form an eigenvalue problem. For a preliminary estimation, the parameters in (13)–(15) for the momentum and density equations may be treated as the same. That is to say, we may let $K_T = K_M = K$, $\nu_T = \nu_M = \nu$, and $C_T = C_M = C$. This way $i\omega + k^2 K + C$ is the eigenvalue of the system and thus the problem can be solved easily.

[10] We have the following observations on the eigensystem (13)–(15): (1) the Newtonian damping C appears in tandem with $i\omega$ and hence inhibits the growth of disturbances; (2) dissipation/diffusion K inhibits temporally growing modes, as for real k, k^2 is always positive, and hence $k^2 K$ somewhat functions like C, albeit not identical (since k also appears on the right hand sides of the equations); 3. when spatial growth is considered, i.e., when k is complex, it might be possible that $k^2 K$ turns negative, and hence facilitates perturbation growth. Of course, this is possible only when K is huge.

[11] Notice that the sign change of the growth rate $Re\{i\omega\} = -\omega_i$ entails a qualitative change of the flow, from unstable to stable or the opposite. Thus, the damping coefficient C is very critical; it may give rise to a fundamental change of the dynamics of the model. The eddy dissipation/diffusion in the momentum or tracer equations is usually small in comparison to other terms. For a length scale of 25 km, and a K typical for the IFF region, the horizontal Ekman number is of the order of 10^{-3}. The vertical Ekman number is also of the same order. The instability hypothesized in (3) is therefore almost impossible for the above system made of momentum and tracer equations, where K plays a very limited role. However, things may be quite different if the vorticity equation is considered, where dissipation carries much more weight in the budget. *Held et al.* [1986] and *DelSole* [1997] have found that dissipation may indeed trigger absolute instability. We will see such an example later in section 5.

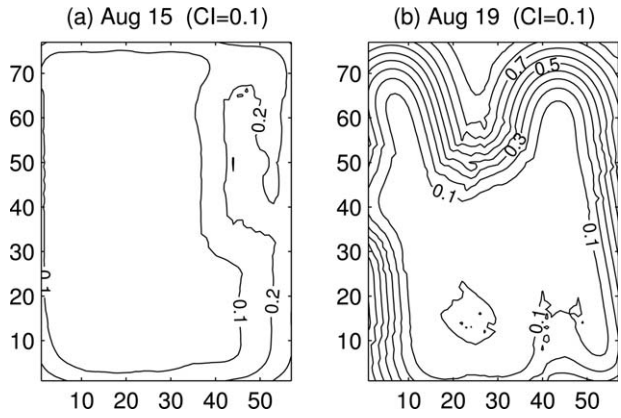

Figure 3. The nondimensionalized observational error of the temperatures (scaled by its maximal value) for (a) 15 August and (b) 19 August. The contour interval is 0.1.

3. Instability Analysis and Parameter Setting with the IFF Variability

3.1. Observational and Gridded Data

[12] The IFF93 data set was acquired from the R/V *Alliance* cruise in a rectangular domain centered at 64.25°N, 10.75°W (Figure 1), with a zonal extent of 140 km and a meridional extent of 190 km. The cruise began on 14 August 1993, and lasted to 23 August. During the 10 day period three surveys were conducted. They are, as named for convenience by *Robinson et al.* [1996], the *initialization survey* (14–16 August), the *zigzag survey* (18–20 August), and the *validation survey* (20–23 August). The initialization and validation surveys are intended for the forecast initialization and validation, respectively. The zigzag survey, which earns its name from its zigzag cruise track, samples adaptively the domain to glean more close-up information

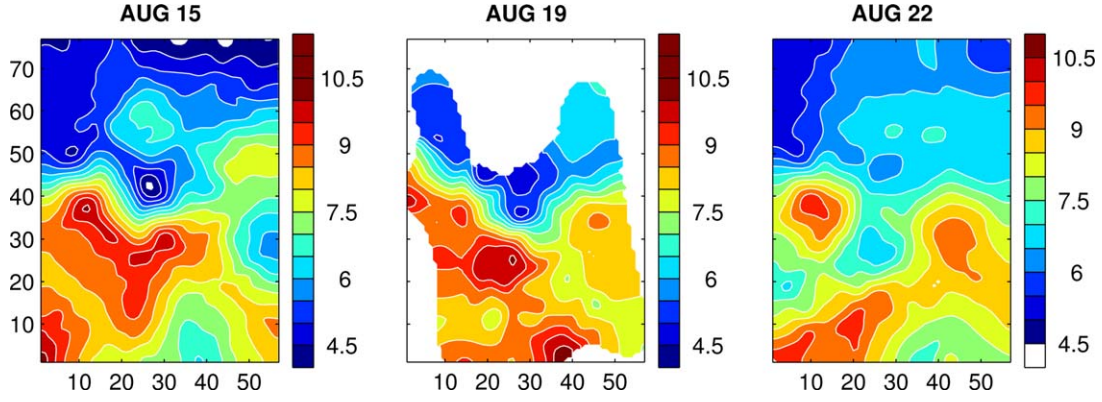

Figure 2. OA maps of the observed 25 m level temperature on the mesh grid for (left) 15 August 15, (middle) 19 August, and (right) 22 August 1993, corresponding to the initialization, zigzag, and validation surveys, respectively. In the middle figure, only regions within tolerable errors (25% of the maximal variance) are shown. All the units are in °C.

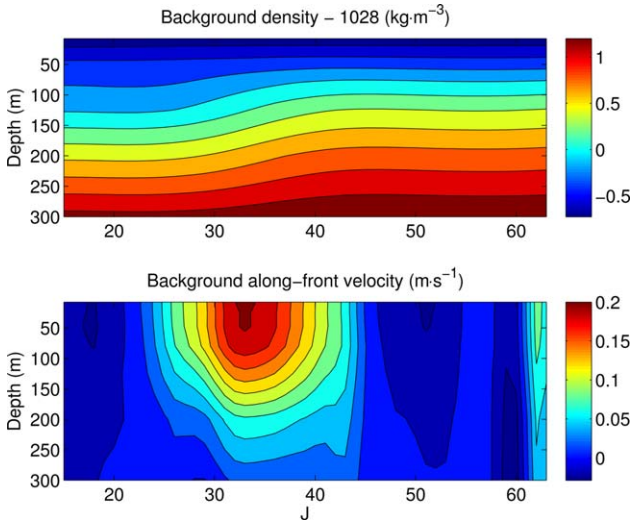

Figure 4. Basic profile for the instability analysis. Upper: density anomaly (in kg/m^3); lower: zonal velocity (in m/s). The abscissa J is the y grid index.

about the meandering stream in the vicinity of the frontal axis.

[13] The obtained data are quality-controlled and preprocessed for the forecasting; for details, refer to *Robinson et al*. [1996]. They are mapped onto an Arakawa B-grid [*Arakawa and Lamb*, 1977] which we have used in *Liang and Robinson* [2004]. It has a domain horizontally discretized into 56 × 76 mesh boxes (57 × 77 grid points), with an equidistant spacing $\Delta x = \Delta y = 2.5$ km. Vertically a hybrid coordinate system is used. Above a depth $H_c = 150$ m, the grid has $k_c = 5$ flat or z levels; below are four terrain-following or σ levels. The thicknesses of the resulting vertical boxes are, from top to bottom, 15, 20, 25, 40, 50, 78, 156, 224, and 312 m (the last four are for reference). Accordingly, the top five z levels are at, respectively, 7.5, 25, 47.5, 80, and 125 m.

[14] The objective analysis, or OA for short, is used to map the data onto the grid. In this study, we use the two-stage OA proposed by *Lozano et al*. [1996] to fulfill the analysis. Shown in Figure 2 are the OAed temperatures for the initialization survey (centered on 15 August), zigzag survey (19 August), and validation survey (22 August), which are generally the same as those of *Robinson et al*. [1996]. Clearly, the three surveys have captured the snapshots of a cold tongue intrusion across the front in the middle of the domain during the experiment. The meandering process by observation can be briefly summarized as a straightening toward the southeast on 19 August, followed by a sudden meandering in a deep-sock or hammer-head form on 22 August (cf. the inserted satellite image in Figure 1). These OAed fields, together with the associated error fields (Figure 3), are to be used later for data assimilation and validation. Note that in computing the errors, it has been assumed that the variability scales are larger than the spacing between cruise station locations; the small scale features shown in the satellite image in Figure 1 are not considered here.

3.2. Instability Analysis With the IFF Model

[15] The instability model (13)–(15) is set up with the gridded data. By the result of *Liang and Robinson* [2004], the convective instability initially takes place near the western boundary, which introduces disturbances into the interior. Naturally, it would be convenient to choose from the OAed observational data a section along the western boundary as the basic profile. But these data before assimilated into the model may not be consistent with all of the model dynamics. We hence instead use the nowcast data just after the initialization on 16 August, i.e., the flow with all the initial data assimilated (see section 4). The parameters needed for the nowcast can be chosen rather freely at this stage; it will be fine provided that they appear reasonable, and the resulting profiles are essentially the same. Since the conditions are persistent at the inflow boundaries (cf. section 4), the profile at the western boundary precludes the possibility of instability (the growth rate is always zero or negative); besides, the hydrocasts are not exactly at the boundary (about three grid points inside). We hence choose a north-south section three grid points to the east (i.e., section I = 3). The so-obtained density and velocity profiles are shown in Figure 4.

[16] For simplicity, only the depths above 300 m are considered. This is justified by the observation that the along-front flow is mainly above 250 m (cf. 4). Likewise, the points beyond the meridional extent $J = 15$–64 are discarded to avoid the effects from the northern and southern open boundaries, Ideally, (13)–(15) should be discretized on the same grid as above (with a sigma-coordinate in the vertical direction). But the main purpose of this instability analysis is for parameter estimation; we are seeking an estimate, not an accurate determination, of the parameters. So the more simple the instability model, the better. We hence discretize the equations on Cartesian coordinates, with the vertical depths at 7.5, 25, 47.5, 80, 125, 200, and 300 m, respectively. Note the top five depths are precisely the same as those for the forecast model.

[17] There are three groups of parameters to tune in equations (13)–(15): Newtonian damping coefficient, vertical viscosity/diffusivity, and horizontal viscosity/diffusivity. If those, respectively, in the tracer and momentum equations are counted as one, they become three parameters, written C, ν, and K. In the HOPS, they correspond to boundary and temporal relaxations, eddy viscosity/diffusivity, and Shapiro filtering; in total there are six parameters for the momentum equations and another six for the tracer equations. The Newtonian damping coefficient $C_M = C_T = C$ always appears in tandem with the growth rate, and they may be viewed as a whole in the dispersion relation. The vertical viscosity/diffusivity $\nu_T = \nu_M = \nu$ essentially has no visible effect on the instability structure, as estimated in the preceding section. (We have tested this,

Table 1. Effective Eddy Viscosities (in m^2/s) for Different Wavelengths and Filter Triplets

Wavelength	25 km	35 km	50 km	100 km	150 km
(*pqr*): (211)	415	215	106	26	11
(*pqr*): (221)	828	429	212	53	23

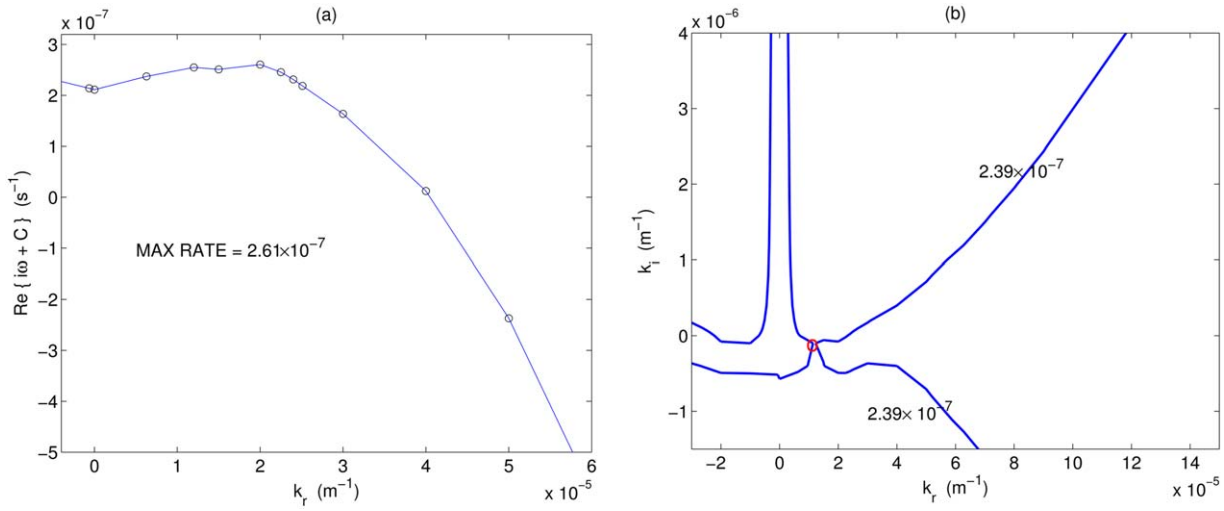

Figure 5. The dispersion relation for $K = 100$ m^2/s. (a) $Re\{i\omega + C\}$ versus k_r. (b) The saddle point in the complex k plane, where absolute instability takes place.

and it is indeed true.) Here it is simply set to be 5×10^{-4} m^2/s. The only parameter that merits mentioning is K_M/K_T, namely, the horizontal eddy viscosity/diffusivity. In HOPS, the eddy dissipation and diffusion are parameterized using Shapiro filters [*Shapiro*, 1971]. A Shapiro filter is represented by a triplet (p, q, r), where p is the filter order, q the frequency of applications per time step, and r the number of time steps between applications, The equivalence between Shapiro filtering and Laplacian diffusion can be demonstrated with a single wave with wave number κ. In this case, a Shapiro filter with a parametric triplet (p, q, r), i.e., a combination of filter order, frequency of application, and number of time steps between applications, has an equivalent effect as an effective eddy diffusion with diffusivity [*Lermusiaux*, 1997, p. 136; *Lermusiaux*, 1999]

$$K = \left[1 - (1 - s^p)^{q/2r}\right] \frac{K_0}{4s},$$

where $K_0 = (\Delta x)^2/\Delta t$, $s = \sin^2(\kappa \mathrm{d}x/2)$. In our model, $\Delta x = 2500$ m, $\Delta t = 180$ s. Choose two triplets (p, q, r) = (2, 1, 1) and (2, 2, 1). The resulting effective eddy viscosities (in m^2/s) for different wavelengths are tabulated in Table 1. Here $r = 1$ is a natural choice; p is set to be 2 because higher order filters (like $p = 4$) blow up the integration. (In fact, for a scale of 25 km, a filter (4, 1, 1) gives an effective viscosity only 3.7 m^2/s, in contrast to the 415 m^2/s as shown above when $p = 2$.) Previously *Hansen and Meincke* [1979] and *Willebrand and Meincke* [1980] estimated that $K = 300$ m^2/s. This corresponds to our result for a wavelength of 30 km when a filter (2, 1, 1) is adopted. Since K varies with wavelength, in the following we test several different cases: $K = 500$, $K = 300$, $K = 100$, and an extreme case $K = 10$ (all in m^2/s).

[18] First choose the well-accepted case, $K = 300$, and solve the corresponding system (13)–(15) for eigenvalues. The dispersion relation we will be plotting is that for $i\omega + C$ versus $k = k_r + ik_i$. We are particularly concerned about

$$Re\{i\omega + C\} = Re\{i\omega\} + C = -\omega_i + C$$

because $Re\{i\omega\}$ is the growth rate of the system. Figure 5a shows the variation of $Re\{i\omega + C\}$ versus the real wave number k_r. The maximum 2.61×10^{-7} s^{-1} is also the maximum attainable for growing modes. Denote this quantity as R_{max}. The maximal growth rate is thence $R_{max} - C$. In the complex plane $k_r - k_i$ the saddle point(s) of the $Re\{i\omega + C\}$ contour lines can be identified; from Figure 5b it is with the contour of 2.39×10^{-7}. This corresponds to the absolute instability, as proved by *Briggs* [1964] [see *Huerre and Monkewitz*, 1990]. For convenience, this quantity is denoted as R_{abs}.

[19] Next consider the other two cases. When $K = 500$, the dispersion relation bears a similar structure as that for $K = 300$, but with smaller growth rates: $R_{max} = 2.42 \times 10^{-7}$ and $R_{abs} = 2.37 \times 10^{-7}$. Likewise, if K is decreased to 100, same thing happens but with larger growth rates ($R_{max} = 3.83 \times 10^{-7}$, $R_{abs} = 3.6 \times 10^{-7}$). But if K is made very small, drastic change may take place. When $K = 10$,

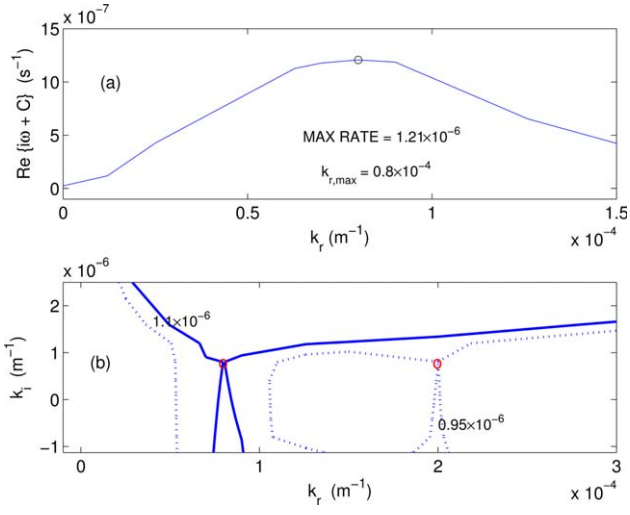

Figure 6. The dispersion relation for $K = 10$ m^2/s. (top) $Re\{i\omega + C\}$ versus k_r. (bottom) The saddle points in the $k_r - k_i$ plane, where absolute instabilities take place.

Table 2. Model Parameters for the Standard Run

Parameters	Value
Model Configuration and Mesh Grid	
Grid	$57 \times 77 \times 9$
Mesh	140 km × 190 km
Time steps for velocity, tracer and transport stream function	180 s
Horizontal grid spacing (Δx and Δy)	2.5 km
Vertical grid spacing	
Horizontal levels 1–5	15, 20, 25, 40, 50 m
Sigma levels 6–9 (reference thicknesses)	78, 156, 224, 312 m
Shapiro Filters (p, q, r)	
Velocity	(2, 1, 1)
Tracer	(2, 1, 1)
Vorticity	(2, 2, 1)
Transport stream function	No application
Boundary Relaxation	
Spatial e-folding distance d_s for	
Velocity	0.7 grid point
Tracer	0.8 grid point
Temporal e-folding distance τ_s for	
Velocity	12,000 s
Tracer	24,000 s
Friction Parameters	
Vertical eddy viscosity ν_M	5×10^{-4} m^2/s
Vertical eddy diffusivity ν_T	5×10^{-4} m^2/s
Bottom drag coefficient	2.5×10^{-3}

we see from Figure 6 that there are actually two saddle points. The left one corresponds to the contour line $1.10 \times 10^{-6}\text{s}^{-1}$ (solid), the right to $9.50 \times 10^{-7}\text{s}^{-1}$ (dashed). In this case, we need only consider the former, i.e., the larger, which corresponds to the most unstable modes. That is to say, $R_{abs} = 1.1 \times 10^{-6}\text{s}^{-1}$. From these results, all the growth rates are of the same order as those for $K = 300$ (in fact, within 5 times in variation) and, as we will see soon in the following, essentially do not make much difference for our purpose of parameter setting. This is what one would like to have, considering that K in this model is not a constant, but depends on the scales of the underlying process(es).

3.3. Parameter Setting

[20] The dispersion relation result, i.e., the growth rates with $\nu_M = \nu_T = 5 \times 10^{-4}$ m^2/s and $K_M = K_T = 300$ m^2/s, determines how the τ_s and d_s in the Newtonian damping coefficient

$$C_M = C_T = C(d) = \frac{1}{\tau_s} e^{-(d/d_s)^2},$$

where d (in grid points) is the distance from the western boundary, should be set. (Once again, here we are actually looking for the stability properties of the front with a fixed C; we are not really taking C as a function of x.) First, at the western boundary, i.e., at $d = 0$, the system must be stable, in consistency with the persistent boundary conditions (until new data come in). We thence must have $R_{max} - C(0) \leq 0$, i.e., the maximal growth rate should be less or equal to zero. This yields

$$R_{max} - \frac{1}{\tau_s} \leq 0,$$

which together with the requirement $\tau_s > \tau_c$ for some threshold τ_c from Appendix A forms a constraint for τ_s:

$$\tau_c < \tau_s \leq \frac{1}{R_{max}}. \tag{18}$$

[21] For the interior points, we require that (1) the flow is unstable in the western region; (2) the instability is convective. Here the statements are definite except for "western region." By what was shown before, the meandering is formed from an instability introduced from upstream, so, ideally, the "western region" should be at the western boundary (i.e., $d = 0$). However, because of the persistent inflow condition, it must be stable there. What about one grid point inside? It might be an appropriate choice; the only concern is still with the clamped boundary nearby. To ask a system stable at $d = 0$ to lose its stability at $d = 1$ imposes too much shock, and make the numerical scheme prone to divergence. For these reasons, we set $d = 2$ in expressing the above statements. Statement (1) is, therefore, $R_{max} - C(2) \geq 0$, or

$$R_{max} - \frac{1}{\tau_s} e^{-(2/d_s)^2} > 0, \tag{19}$$

and statement (2) reads: $R_{abs} - C(1) \leq 0$, i.e.,

$$R_{abs} - \frac{1}{\tau_s} e^{-(2/d_s)^2} \leq 0. \tag{20}$$

Solving these two inequalities for d_s, one obtains

$$\frac{2}{\sqrt{-\log(\tau_s R_{abs})}} \leq d_s < \frac{2}{\sqrt{-\log(\tau_s R_{max})}}. \tag{21}$$

So actually the tuning of d_s depends on τ_s and R_{max} and R_{abs}, the latter two being functions of $\overline{u}$, $\overline{\rho}$, K, and ν (ν essentially makes no effect here).

[22] From the inequalities (18) and (21) we may set τ_s and d_s. Plug $R_{max} = 2.61 \times 10^{-7}$ into (18) to get $\tau_s < 3.8 \times 10^6$ s. This essentially sets no upper bound for τ_s (the lower bound is τ_c), since in this case usually it is of an order of several hours; otherwise the boundary effect will never enter into the interior. We may therefore pick freely a τ_s that sounds reasonable. Let $\tau_s = 12{,}000$ s. Substitution of $R_{max} = 2.61 \times 10^{-7}$ and $R_{abs} = 2.39 \times 10^{-7}$ into (21) gives

$$0.82 \leq d_s < 0.83.$$

This is really remarkable, as it gives us an almost exact value: $d_s = 0.82$, while our estimation is just in an approximate sense! Indeed, as one will see soon, when $\tau_s = 12{,}000$, and a filter (2, 1, 1) is used, d_s should be chosen around 0.8 to get the best forecast.

[23] Of course, one may argue that, in forming the mathematical statements, d could be a number other than 2. This is, indeed, a rather subjective issue. What we can say is,

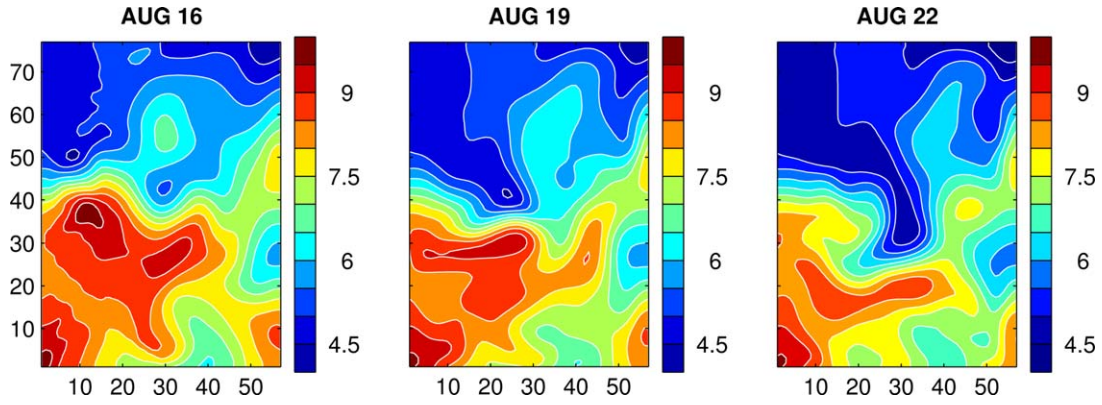

Figure 7. F2 forecast of the 25 m temperature for day 2 (16 August), day 5 (19 August), and day 8 (22 August).

since the convective instability is ushered from the west, in forming statement (1), the closer to the western boundary, the more physically reasonable. So in (19), $d=2$ could be the best. (As argued before, d should not be set 1 to avoid shocking the system.) But it is not impossible that the instability frontier could be extended further inside to some $d=m$; m can be determined by the lower bound of the typical scale in the region. In this case, statement (1) becomes

$$d_s < \frac{m}{\sqrt{-\log(\tau_s R_{max})}}.$$

From previous studies, e.g., *Smart* [1984], *Willebrand and Meincke* [1980] and *Allen et al*. [1994], to name a few, the scale could be as small as 10 km, which results in $m=4$. $\frac{4}{\sqrt{-\log(\tau_s R_{max})}}$ is thus the upper bound for d_s, given τ_s and the growth rates. To obtain the lower bound for d_s, consider $d=1$. As mentioned above, we cannot impose here the instability requirement, i.e., statement (1). The system might be stable or unstable. Nonetheless, one thing is for certain, it must NOT be absolutely unstable (i.e., only convective stability is allowed), otherwise it would give a premature intrusion. That is to say, $R_{abs} - C(1) \le 0$, or

$$R_{abs} - \frac{1}{\tau_s} e^{-(1/d_s)^2} \le 0.$$

These put together yield,

$$\frac{1}{\sqrt{-\log(\tau_s R_{abs})}} \le d_s < \frac{m}{\sqrt{-\log(\tau_s R_{max})}}, \qquad (22)$$

where $m=4$ in this study. This may be understood as an estimate of the range of sensitivity for d_s, given τ_s and the growth rates. Substituting for the above numbers, this is (0.41, 1.66). Later on in section 5, one will obtain an approximate range of (0.5, 1.5) by sensitivity studies. Again, this is a remarkably accurate estimate,

[24] If τ_s is doubled to 24,000, (22) becomes $0.44 \le d_s < 1.78$. When $\tau_s = 5000$ and 50,000, the ranges are, respectively, [0.39, 1.56) and [0.48, 1.92). So we may choose τ_s rather freely between 5000 and 50,000, and the resulting d_s will not make much difference. Since R_{max} and R_{ab} appear in the inequality in a product with τ_s, it is expected that the change of K will not make much difference in d_s, either. Indeed this is true. For the cases $K=10$ and $K=500$, the resulting R_{max} and R_{abs} will, by calculation, give similar constraints.

[25] To summarize, the vertical mixing parameter ν essentially has very little effect on the dynamics. The temporal e-folding time τ_s can be chosen rather freely between 5000 and 50,000. The effect of filtering is not significant, either, and one may choose a triplet such as (2, 1, 1) or (2, 2, 1). A dynamically consistent spatial e-folding distance d_s is constrained by (22), which depends on τ_s and the filter adopted. A more stringent constraint is (21), which, for $\tau_s = 12{,}000$ (in seconds), gives a rather accurate estimate of d_s around 0.8 (in grid points). Since in the HOPS there is another equation namely the barotropic vorticity equation to solve, and by experimentation it requires some extra filtering to ensure numerical stability, the d_s for momentum is lowered slightly to 0.7 by compensation. Considering that tracers usually respond more slowly to perturbations than velocity fields, the τ_s for the former is doubled. As a summary these and other parameters are listed in Table 2.

4. Forecasting the IFF Large Meandering

[26] With the above parameters we perform the forecast. The forecasting strategy, including initialization, sequential data updating, etc., is referred to *Robinson et al*. [1996]. For reference convenience, 14 August may be referred to as day 0, 15 August as day 1, and so on. As the first step,

Table 3. F2 Forecast Skill Versus Persistence (Assimilating 16 August/Predicting 22 August)

Level	ACC Change	RMSE
7.5 m	+0.206	−14.0%
25 m	+0.171	−2.5%
47.5 m	−0.036	+21.7%
80 m	−0.062	+32.1%
125 m	+0.033	−1.5%
σ_6	+0.108	−31.6%
σ_7	+0.014	−47.8%
σ_8	+0.012	−45.3%
σ_9	0	−15.8%

Table 4. A Few Experiments Mentioned in the Text

	Filtering			Boundary Relaxation		Frc	
Run	Momentum	Tracer	Vorticity	Momentum	Tracer	ν_M, ν_T (cm^2/s)	Remarks
1	(211)	(211)	(221)	(0.7, 12,000)	(0.8, 24,000)	5, 5	Standard experiment
2	(211)	(211)	(221)	(0.7, 12,000)	(0.8, 24,000)	0.5, 0.5	Similar to Run 1
3	(211)	(211)	(221)	(0.7, 12,000)	(0.8, 24,000)	15, 15	Similar to Run 1
4	(411)	(411)	(421)	(0.7, 12,000)	(0.8, 24,000)	5, 5	Blows up
5	(212)	(212)	(211)	(0.7, 12,000)	(0.8, 24,000)	5, 5	Blows up
6	(221)	(221)	(221)	(0.7, 12,000)	(0.8, 24,000)	5, 5	As Run 1 but with small-scale features smoothed
7	(241)	(241)	(221)	(0.7, 12,000)	(0.8, 24,000)	5, 5	Same as above
8	(241)	(241)	(241)	(0.7, 12,000)	(0.8, 24,000)	5, 5	Result very different
9	(221)	(221)	(241)	(0.7, 12,000)	(0.8, 24,000)	5, 5	Integration blows up
10	(211)	(211)	(221)	(1.5, 12,000)	(1.5, 24,000)	5, 5	Meander okay, but for geometry
11	(211)	(211)	(221)	(3, 12,000)	(3, 24,000)	5, 5	No deep-sock meandering (cf. Figure 8b).
12	(211)	(211)	(221)	(0.4, 12,000)	(0.4, 12,000)	5, 5	Blows up
13	(211)	(211)	(221)	(0.7, 50,000)	(0.8, 50,000)	5, 5	Similar to Run 1
14	(211)	(211)	(221)	(0.7, 7500)	(0.8, 7500)	5, 5	Similar to Run 1

only the data from the initialization survey (day 0 through day 2) are utilized for the forecast. We will call this the F2 forecast henceforth, adopting a convention used before by *Robinson et al*. [1996]. The zigzag data will be dealt with later in section 6, and the corresponding forecast will be termed the F5 forecast.

4.1. The F2 Forecast Result

[27] The F2 forecast result is shown in Figure 7, where three snapshots of the 25 m temperature are plotted, in correspondence to that of Figure 2. The nowcast for day 2 reveals a front running wavely east-westward between approximately $J = 35$ and $J = 45$. Its strength decreases from west to east, with a like structure and position throughout the water column. In the upper layer, two warm centers sitting immediately south of the front; in deep layers, this bicenter structure gives way to a sole strong warm center in the west (not shown).

[28] On day 5, the western frontal axis is reoriented and becomes straightened southeastward. Accompanied is a strong current toward the southeast. This event has been captured by the model throughout the water column, and is particularly evident on the surface and middle levels. The warm centers identified south of the front on the day 2 patterns show a clear evolution. At depth 25 m, the one in the west disappears; at depth 300 m, the unicenter evolves into a dipole structure (not shown). This evolutionary trend is clearly seen in the OA maps in Figure 2. The dynamical processes have been qualitatively correctly reproduced in the day 5 forecast.

[29] The day 8 forecast is the target of this study. Comparing the temperature distribution of Figure 7 to that of Figure 2, the predicted meander is correlated well to the observation, both in spatial location and in geometry. Particularly appealing is the way the meander is oriented. The cold water intrudes westward, in good agreement with both the satellite image (cf. 1) and the in-water observation. Besides, some indication of scale-similarity, which is lacked in the OA maps (Figure 2) because of the sampling resolution but is present in the AVHRR image (Figure 1),

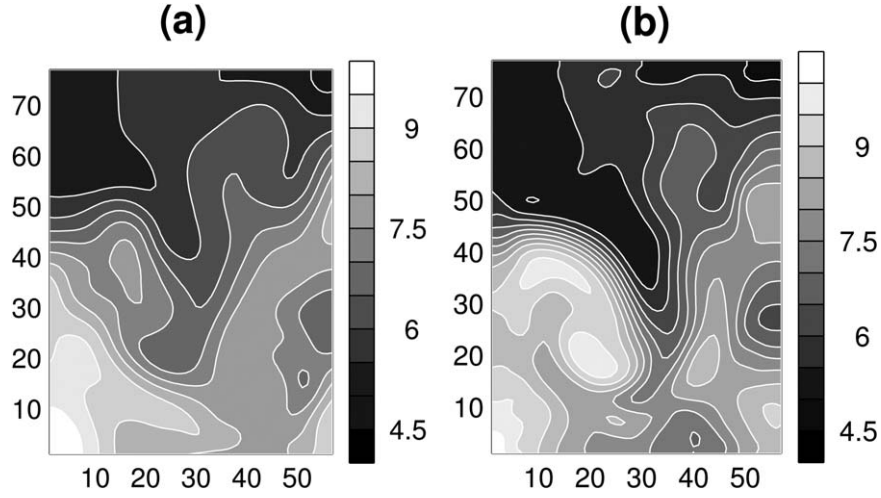

Figure 8. The 25 m temperature on day 8 (22 August) predicted (a) with Shapiro filters (2, 4, 1), (2, 4, 1), (2, 4, 1), respectively, for momentum, tracer, and vorticity equations, and (b) with a boundary relaxation $d_s = 3$ points for both momentum and tracer equations.

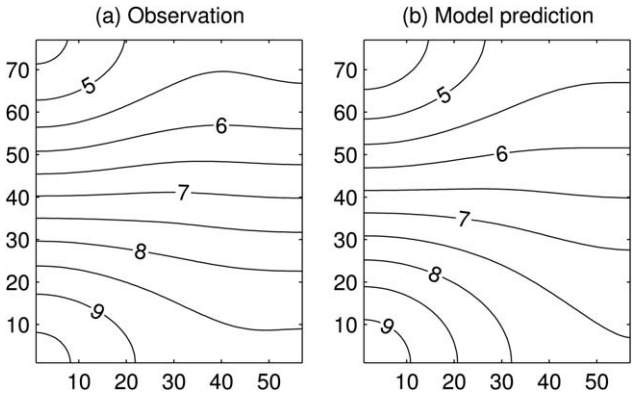

Figure 9. The large-scale temperature distribution reconstructed with (a) observation, and (b) model prediction for the fifth forecast day. A window index $j_0 = 1$ is used for the 2-D cubic spline scaling basis [*Liang and Anderson*, 2007].

is significant in the details of the meandering shape; the cooler tongue intrusion from the northwestern corner, which is seen in the satellite image but not in the OA map because of the sampling resolution, is also clearly seen here.

[30] The inaccuracies of the forecast are also easily seen. On 19 August, the strength and extent of the front straightening are not enough. The slope is too mild to be quantitatively comparable to that of Figure 2. Also not enough is the cross-front temperature gradient. A direct consequence is that the along-front current is too small. The maximal speed along the front axis is 69 cm/s (figure not shown), about 10 cm/s less than the 79 cm/s inferred from the surface drifters [*Miller et al*., 1995a, 1995b]. Apart from that, two cold centers in the east on 16 August persist through the experiment, an event not seen in the OA sequence. Obviously, this is due to the persistent boundary conditions that cannot be resolved unless new data come in. On 22 August, the predicted meander lies too much eastward; the front is not strong enough on the western flank; the isolines, particularly the 9°C isoline, do not crest up much to make a round shaped hot center immediately west of the meandering. Besides, the predicted meandering intrusion slightly lies to the north, a problem which could result from the mild day 5 straightening, and should be alleviated by assimilating the zigzag data (cf. section 6).

[31] It would be interesting to give the forecast a quantitative evaluation. As discussed in the literature [*Peloquin*, 1992, cf. the special issue of *Oceanography* 1992 edited by R. A. Peloquin], the mesoscale forecast skill may be measured by anomaly correlation coefficient (ACC) and root-mean-square error (RMSE):

$$\mathrm{ACC} = \frac{\overline{T'_p T'_o}}{\left(\overline{T'^2_p}\,\overline{T'^2_o}\right)^{1/2}},$$

$$\mathrm{RMSE} = \overline{\left(T_p - T_o\right)^2}^{1/2}$$

versus persistence. In these equations, overline stands for an averaging over some designated space domain, prime for deviation from the average, and the subscript p and o for "prediction" and "observation," respectively. In this study, the scalar field T is temperature, and by "observation" we mean the data mapped with OA into the mesh grid. Clearly, a high forecast skill must have a high ACC and a low RMSE. One may then use the ACC and RMSE of forecast versus the ACC and RMSE of persistence to score the forecast skill. Table 3 lists the calculated forecast skills against persistence for the validation domain (a rectangle 11.6–9.9°W, 63.8–64.5°N). From the numbers one can tell that the ACC for all the levels are increased, except for levels 3 and 4, and the σ level 9. Correspondingly, the RMSE drops at all levels, except for levels 3 and 4. The ACC changes most drastically at the surface levels (levels 1 and 2), but the largest RMSE decreasing happens in deep layers (sigma levels 6, 7, and 8). Taking all these into account, levels 1 and 6 (sigma) score the highest, and levels 2, 7, and 8 the second. Through the water column only levels 3 and 4 do not score as expected.

[32] In summary, the F2 forecast has faithfully reproduced the processes for the IFF to evolve into an almost detached meandering. By visual inspection, the two major events, the southeastward straightening, and the deep-sock meander intrusion, have been satisfactorily predicted, either in terms of strength, geometry, and orientation. The prediction has also been quantitatively scored in terms of ACC and RMSE against persistence, and the score is generally satisfactory, particularly for the surface and deep levels.

5. Sensitivity Studies

[33] As shown above, a faithful reproduction of the two phases of a baroclinic instability, i.e., the convective instability and the absolute instability, and the timing of the phase switch, is crucial in forecasting the observed IFF meandering intrusion. We have conducted over 90 experiments to test the F2 forecast against parametric sensitivity; these sensitivity studies have further confirmed this rule of thumb. This section summarizes briefly the major results of these studies. A few experiments mentioned in the text are listed in Table 4, among which the first is the one described above, i.e., the standard run.

5.1. Vertical Viscosity and Diffusivity

[34] In section 2, we conjectured through a preliminary estimation that the two vertical mixing parameters, ν_M and ν_T, may not exert much effect on the instability structure and hence the meandering intrusion. Indeed this is true. In the standard run, they are both chosen as $\nu_M = \nu_T = 5$ cm^2/s. Reducing the value by more than an order to 0.5 cm^2/s yields a result without any visible difference (run 2 in Table 4); on the other hand, incrementing it to 15 cm^2/s does not affect the outcome, either (run 3). The forecast is therefore insensitive to the changes of vertical eddy viscosity and diffusivity within their respective bounds.

5.2. Filtering

[35] In the HOPS, Shapiro filters are employed, for one thing, to ensure numerical stability and, for another, to parameterize the subgrid processes of the horizontal mixing. The triplet for the above standard run is by experiment an optimal one. As shown in Table 4, higher order (run 4) or less (run 5) filtering causes energy to build up at the grid

scale which eventually blows up the integration. To test the sensitivity, a vast variety of runs have been performed with different triplets. Generally, once the scheme is stabilized, the mesoscale meandering is insensitive to the change of (p, q, r) for the momentum and tracer equations, just as estimated in section 2. Changing run 1 to run 7, the application frequency q is increased from 1 to 4, correspondingly the effective viscosity is increased from 400 to 1600 m^2/s for of 25 km waves, and from 20 to 100 m^2/s for 100 km waves. The results, however, are essentially the same, only with the small-scale features smoothed out.

[36] Besides the momentum and tracer equations, the HOPS has an additional vorticity equation to solve for the barotropic fields [see *Lozano et al*., 1996]; the resulting barotropic vorticity is inverted to obtain the transport stream function, barotropic pressure, etc. Shapiro filters are also employed to parameterize the subgrid processes. Different from the above tests with momentum and tracer, here if the application frequency q is increased from 2 to 4, dramatic change is seen in the final result (runs 8 and 9 versus runs 6 and 7). Shown in Figure 8a is the predicted 25 m temperature for day 8 using the filters in run 8. Apparently, the flow is very unstable near the western boundary, giving to a pattern quite different from the prediction in the standard run. A deep study may be made by applying the new mathematical machinery multiscale window transform (MWT hereafter) of *Liang and Anderson* [2007] and the MWT-based localized hydrodynamic stability analysis [*Liang and Robinson*, 2007] to the forecast fields, following what we did in *Liang and Robinson* [2004] and using the same parameters therein. The instability problem is reduced to the finding of a quantity called *canonical transfer* (previously called perfect transfer in *Liang and Robinson* [2007]), which quantitatively gives the nonlinear growth rate local in space and time. By examining the calculated canonical transfer from the large-scale window (longer than 5 days) to the mesoscale window (about 1–5 days) for day 4 and day 6, we find that the transfer center stays still near the western boundary (not shown). This is in contrast to what we have observed in *Liang and Robinson* [2004, Figure 9], where the hotspot has moved into the interior by day 6. The implication of this change is that in run 8 the stage of convective instability is prematurely turned off before an absolute instability takes over. In other words, the heavy dissipation of vorticity makes the system absolutely unstable near the western boundary, which is otherwise convectively unstable. This spurious instability-caused grid-sized oscillations near the western boundary cannot be damped out without heavy momentum and tracer filterings, and that is the reason why the integration in run 9 blows up.

[37] That dissipation may trigger absolute instability in a flow which would be otherwise stable or convectively unstable has been discovered before by *Held et al*. [1986] and *DelSole* [1997]. The possibility is also seen from the dispersion relation in section 2. But, as estimated there and demonstrated above in the experiments, the eddy dissipation (resp. diffusion) for the momentum (resp. tracer) equations (within physically reasonable bounds, of course) is not strong enough to make a sizable contribution to the dispersion relation. How come the vorticity dissipation functions so differently? In the analytical instability model, we avoid solving the vorticity equation for pressure or pressure-related fields by assuming an inert deep layer. In the hidden vorticity equation, only one term is planetary vorticity-related, that is, the β-effect term, thank to the nondivergent transport. Let us do a quick dimensional analysis. Denote as ν_{vor} the eddy vorticity viscosity, and let $\nu \sim U$. Then the β-effect is of the order of 10^{-11} U, while $\nu_{vor}\nabla^2\zeta \sim \nu_{vor} U/L^3$. For a scale of 25 km, the effective viscosity of filter (2, 4, 1) is about 1600 m^2/s, resulting in a vorticity dissipation of the order of 10^{-10} U, which is one order larger than the β-effect! It is no doubt that this huge dissipation may significantly alter the dispersion relation and hence the stability structure.

[38] To summarize, filters for the momentum and tracer equations generally tend to stabilize the integration, and only function to damp small-scale features without changing the mesoscale meandering intrusion. But for the vorticity equation, caution should be used in applying filters because of the delicate balance between dissipation and other mechanisms. Heavy filtering to the vorticity equation may trigger a spurious absolute instability near the western boundary, which results in a premature meandering and an intrusion pattern completely different from that from the standard run.

5.3. Boundary and Temporal Relaxations

[39] The nudging at the open boundaries, which is designed to stabilize the numerical scheme, and to alleviate the ill-posedness of the regional modeling problem, proves to be a key factor that may shatter the stability structure of the flow. We have demonstrated this in section 2, and given a detailed discussion in section 3.3 on the determination of the two related parameters, namely, d_s and τ_s. This subsection is devoted to test the sensitivity against their changes. Listed in Table 4 are five runs among the testing experiments (runs 10–14).

[40] As discussed before, large d_s tends to inhibit the baroclinic instability and hence the meandering intrusion. Fix τ_s (as that for run 1) and let d_s increase. When $d_s = 1$, the result is essentially unchanged. When $d_s = 1.5$ (run 10), the resulting meandering is still fine, but shows discrepancy in its shape. Further increase d_s. After d_s exceeds 2, the instability seems to be inhibited, and no deep-sock or hammerhead meandering appears. Shown in Figure 8b is the predicted 25 m temperature for day 8, the result of run 11 with $d_s = 3$. On the other hand, decreasing d_s to a value below some threshold may yield the convective instability to a premature absolute instability, and hence a premature meandering intrusion. By the calculation in section 3.3 the threshold is around 0.5. To test this, let $d_s = 0.5$; the result is still similar to that from the standard run. Reduce d_s more to 0.4 (run 12). This time, however, sees a divergent integration. Nonetheless, the numerical divergence could be related to a very unstable physical system, which to some extent echoes our premature intrusion conjecture. (Indeed the numerical divergence begins in the western boundary region.)

[41] We have demonstrated in section 3.3 that, in contrast to d_s, the prediction should be insensitive to the change of τ_s. (This is, of course, due to the fact that d_s appears in the exponential power of the Newtonian damping coefficient, while τ_s does not.) Indeed this is true, as shown in runs 13 and 14. Fix d_s as that for run 1 and choose

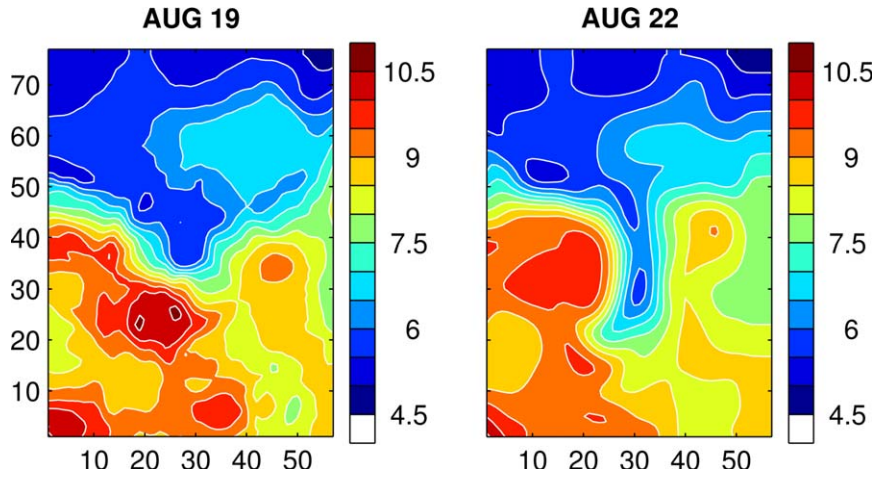

Figure 10. F5 forecast temperature for day 5 (19 August) and day 8 (22 August).

$\tau_s = 50{,}000$ (run 13) and $\tau_s = 7500$ (run 14), and the predictions essentially show no difference from the standard run. We may, therefore, safely claim that the F2 forecast is insensitive to the choices of d_s and τ_s, provided that they are appropriately set so that the underlying physics is represented (e.g., $0.5 < d_s < 1.5$, $7500 < \tau_s < 50,000$, plus the constraint (22)).

6. Zigzag Data Assimilation and the F5 Forecast

[42] As one sees from the above, though qualitatively successful in reproducing the meandering intrusion, quantitatively there still exists some gap between the observation and prediction. This is, to a large extent, due to a lack of data input beyond day 2, and the resulting persistent boundary conditions afterward. Here we show how the zigzag data may come to help in this regard. This section might be a little digression from the main flow; we include it here for the completeness of the forecast. Besides, as we will see soon, the experiments with data assimilation from another aspect reconfirm the previous "rule of thumb."

[43] Before assimilated, the zigzag data are OAed onto the grid on day 5 (19 August). The assimilation is achieved through the classical pointwise optimal interpolation; in the following we will refer to it as OI.

6.1. Two-Scale Data Assimilation

[44] The zigzag data set, which was acquired on 18–20 August, is distinct from the other two sets in that (1) a considerable number of probes did not reach the bottom; (2) it does not contain salinity information; (3) the hydrocasts cover only a part of the domain (see the hydrocast map in *Robinson et al*. [1996]).

[45] We overcome (1) by combining these casts with all the hydrographic data available up to day 6 (20 August) to prepare the assimilation fields, and remedy (2) by *salting* the XBT casts, i.e., augmenting them with consistent salinity information. Salting is now a common practice [e.g., *Sloan*, 1996] in data preparation. It is justified by the observation that temperature and salinity are more often than not statistically highly correlated; a T-S diagram, for example, often allows one property to be derived from the other. The most severe problem arises with (3), which produces an inhomogeneous error distribution, and then may give spurious structures in the fields after assimilation. In Appendix B, we show how these structures arise using a highly coarse-grained model.

[46] This above problem actually originates from the classical optimal interpolation methodology. The scheme is to minimize a performance or cost functional such that the observed field and the model prediction as a whole are combined into a new field. This does nothing to distinguish features of one scale from another. If the error field is not spatially uniform, as exemplified above, spurious structures arise through interscale transfers. In the present study, this problem could be severe, considering that the zigzag error is in a pattern like Figure 3b. The multiscale issue, therefore, must be addressed in devising an appropriate assimilation scheme for the F5 forecast.

[47] An in-depth study of multiscale assimilation is beyond the scope of this study. To cope with the problem we just adopt a simple scheme, a scheme aiming at reducing or removing the C in the example shown in Appendix B (as the error field is not alterable). This is achieved by removing the large-scale part of both the model result and the observation. The two fields that are to be melded are therefore the *de-trended* fields. After the assimilation, the trend (of the model prediction) is added back to get the updated field. In doing so, the potentially spurious structure due to the discrepancy of the predicted and observed large-scale features, if any, is then effectively removed.

[48] The large-scale features, by which we mean here the basin-scale trend, is obtained through reconstruction using a 2-D cubic spline scaling basis [*Liang and Anderson*, 2007], with a spatial scale level index $j_0 = 1$. Figure 9 shows the basin-scale distributions of both the predicted and observed temperatures, $\overline{T}_o$ and $\overline{T}_p$, for the forecast day 5 (19 August). Notice the difference in value (about 0.5°C) albeit the pattern as a whole is similar. This offset would lead to spurious patterns with the zigzag observation errors, should these two basin-scale features be involved in the optimal interpolation. In fact, the thermal wind relation implies

Table 5. Spatially Lagged F5 Forecast Skill Versus Persistence (Assimilating 16 August/Predicting 22 August)[a]

Level	Spatial Lag	ACC Change	RMSE
7.5 m	4 points	+0.176	−29.2%
25 m	4 points	+0.193	−31.1%
47.5 m	0 points	+0.173	−31.7%
80 m	0 points	+0.189	−32.4%
125 m	2 points	+0.150	−25.6%
σ_6	3 points	+0.124	−23.4%
σ_7	6 points	+0.119	−36.2%
σ_8	6 points	+0.173	−50.8%
σ_9	2 points	+0.228	−52.8%

[a]The spatial lag is in x (positive if moved westward).

$$v \sim \left| \frac{g}{\rho_0 f_0} \int_{-H_0}^{0} \nabla \rho \mathrm{d}z \right| \sim \left| \frac{\alpha g}{\rho_0 f_0} \int_{-H_0}^{0} \nabla T \mathrm{d}z \right|, \qquad (23)$$

where $\alpha = \frac{\partial \rho}{\partial T}$, and H_0 the reference depth of no motion. The UNESCO equation of state for seawater [*Millero et al.*, 1980] yields an $\alpha \approx -0.15$ for the typical temperature and salinity in this region. Take H_0 to be 300 m. Substitution of $\rho_0 \sim 1000$ kg/m^3, $g \sim 10$ m/s^2, $f_0 \sim 10^{-4}$ 1/s, $\Delta x \sim 10$ km, $\Delta T \sim C \sim 0.5$ °C into (23) gives a rough estimate of the spurious surface velocity in the order of 0.2 m/s, or 20 cm/s. The flow thus obtained may therefore bear a large error. To overcome this problem, we subtract these basin-scale features from the originals and then apply the pointwise OI on the de-trended structures. Suppose the so-assimilated field is $T_p'^{+}$. The forecast temperature is then updated with $T_p'^{+} + \overline{T}_p$.

[49] With this simple two-scale assimilation scheme is the zigzag data assimilated. In order not to shock the system, it is ramped up from day 4 (18 August) to day 5 (19 August), rather than applied at one time step. In these two forecast days, the assimilation weight ω is increased from 0.50 to 0.99 ($\omega = 1$ means 100% of the observation is taken in).

6.2. The F5 Forecast Result

[50] The F5 result has been reported in *Liang and Robinson* [2004]; below till the next paragraph is just a brief summary. Shown in Figure 10 is the resulting temperature for depth 25 m. Clearly, the assimilation of the zigzag data introduces many small-scale features, scattered on all levels through the water column. These grid-size events are soon dissipated, without affecting the large-scale evolution. Compared to Figure 7, the nowcast on day 5 results in a much steeper front, plus a cold center unseen in Figure 7 in the southwestern corner.

[51] From the day 5 nowcast the front evolves on, and by day 8 a deep-sock meandering intrusion forms (Figure 10, right). As that of the F2 forecast, both the geometry and the orientation of the intrusion are in good agreement with the observation. Significant improvement since the F2 forecast is also seen. In comparison to Figure 7, the front strength is more realistic; all the isolines of temperature on the western flank crest up, just as those observed; the intrusion is farther southward; the high temperature pool on the western flank is faithfully reproduced. Besides, it successfully predicts a cold spot in the southwestern region which does not appear in the F2 forecast.

[52] Quantitatively one would expect that the F5 forecast is also significantly improved. However, the above forecast skill metric does not seem to record the improvement. For a better evaluation the metric need to be modified. This is done by correcting the phase of variation for each level before the ACC and RMSE are calculated [*Robinson et al.*, 1996]; that is to say, we check the agreements except for that in phase. Here we simply have the predicted temperature lag in the x direction by some distance (westward). The lag is on a level-by-level basis. For all those well predicted, no lag is necessary; others like levels 1 and 2, a slightly more lag is needed. The lag distribution is summarized in Table 5 (second column), with grid spacing as the unit. The recalculated ACC and RMSE are shown on the right in the same table. Obviously, the F5 forecast has a high forecast skill score.

[53] We extend the evaluation to times other than day 8 (22 August). Plotted in Figure 11 are the time sequences of the ACC and RMSE for level 4, the very successfully F5 forecast level and the least successful F2 forecast level, from day 5 (19 August) to day 9 (23 August). The dashed lines signify persistence. Both the ACC and RMSE evolutions indicate that the forecast scores highest on day 8, the

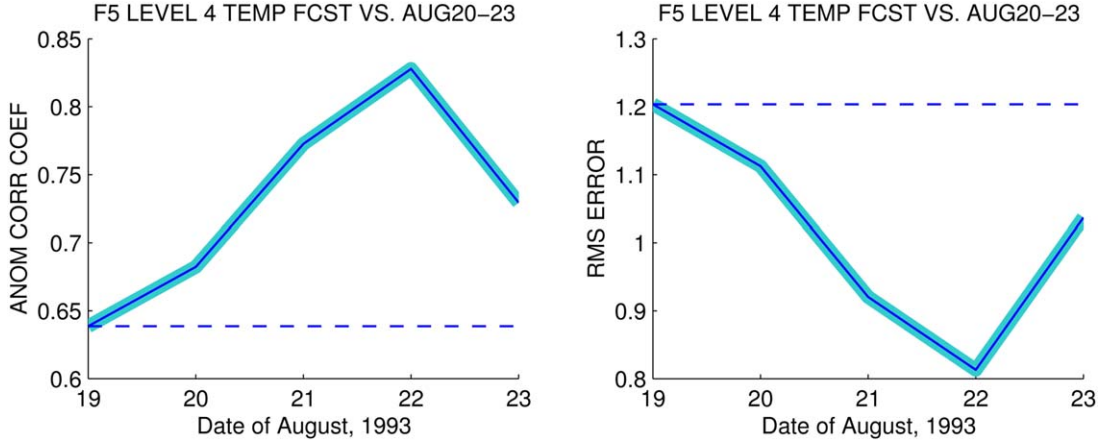

Figure 11. (left) ACC and (right) RMSE for the F5 forecast (solid) versus persistence (dashed).

time when the deep-sock or hammer-head meander matures. After that, the score drops. By *Miller et al*. [1995b], this kind of variation in ACC and RMSE provides a clue of predictability of the problem. By all that account, the forecast skill scores are high for all levels; the results are highly relevant to the observations. Our simulation is therefore satisfactorily validated.

[54] It is of interest to see how the F5 forecast is improved compared to F2 in terms of the underlying dynamics. Applying the MWT of *Liang and Anderson* [2007] and the MWT-based canonical transfer analysis [*Liang and Robinson*, 2007, 2009], using the same parameters as those in *Liang and Robinson* [2004], to both the F2 and F5 fields, we find, from the evolution of the resulting canonical transfers (not shown), that the F2 forecast has reproduced the whole scenario of the baroclinic instability, which appears first as a convective instability, then an absolute instability. Compared to that of the F5 forecast, however, the F2 convective instability is delayed, and both the convective and absolute instabilities are too weak to produce a meandering strong enough as observed. The assimilation of the zigzag data improves the forecast through advancing and strengthening the convective instability, and enhancing the absolute instability that follows.

6.3. A Remark on Data Assimilation Versus Dynamical Processes

[55] The success of the F5 forecast seems to demonstrate that taking in more data will improve the prediction. This is, of course, a common belief, but it is only conditionally true. The first issue is the way how the data are assimilated. We have tested more than 20 experimental runs with different zigzag data assimilation schemes, including schemes without multiscale consideration and schemes with ramp-up and ramp-down strategies before and after day 5. The results are quite different, and are generally not as successful as the F2. That is to say, if the zigzag data are not quality-controlled, and/or not appropriately assimilated, they may not improve the forecast or, in many cases, even make things worse.

[56] A more profound issue usually ignored is with the dynamical processes we emphasized in the beginning. If a model setting does not admit the process(es) that is (are) needed in producing the target phenomenon, in general it is futile for the prediction. In this study, the key process is the convective instability followed by an absolute instability. We test two cases: (1) no linear instability is admissible; (2) the instability at the western boundary is absolute. According to sections 3.3 and 5, a choice of $d_s = 3$ and $\tau_s = 12{,}000$ inhibits the linear instability. With this set of parameters, we relaunch the F5 forecast, using the standard assimilation scheme. As expected, on the resulting 22 August temperature distribution no deep-sock or hammer-head meandering intrusion appears (figure not shown). To test the second case, one may choose $d_s = 0.4$, an e-folding distance below the threshold for absolute instability, but the integration blows up, as in the F2 forecast. We then test with the parameter combination for Figure 8a, where an unexpected absolute instability is triggered by the heavy filtering. Again, the resulting day 8 temperature distribution sees no improvement in comparison with that in Figure 8a. Apparently, data may not always come to help, unless the physics is correctly represented in the model.

7. Discussion

[57] To set up a model such that the underlying physics for the targeting phenomenon is faithfully represented is the key to the success of ocean prediction. In the case of the Iceland-Faeroe front (IFF), for example, dynamically it has been observed to be a convective instability followed by an absolute instability (both are baroclinic), and hence a spatial noise-like amplifier locked into a temporally growing mode [*Liang and Robinson*, 2004]. A physically consistent forecast of the meanderings, thereby, must have these processes reproduced. In this study, we studied the frontal instability properties, and identified the parametric dependencies for the two instabilities, which allow for a physically consistent setting of tunable model parameters. This not only saves enormous (and tedious) effort of experimentation, which is usually a formidable task in numerical modeling, but also provides for us criteria to distinguish a physically relevant forecast from numerical artifacts.

[58] We put the above criteria to application to the forecast of the IFF large meandering observed on 22 August 1993. An instability model is set up with a basic profile of the cross-front section drawn from the real-time data set. By analyzing the model it is found that the convective/absolute instability structure has a major dependency on Newtonian damping, which takes effect jointly with horizontal dissipation. The Newtonian damping-related parameters, i.e., the e-folding temporal relaxation time τ_s and the e-folding relaxation distance d_s (see Appendix A), are hence the most critical parameters to tune. Solving the instability model one obtains a maximal generalized growth rate, i.e., growth rate plus the Newtonian damping coefficient C, and a generalized absolute growth rate, written R_{max} and R_{abs}, respectively. Numerically one must have

$$\tau_c < \tau_s \leq \frac{1}{R_{max}},$$

where τ_c is from Appendix A, for a persistent inflow boundary; from the computed R_{max} this essentially sets no upper bound for τ_s. Dynamically, the process underlying

Table 6. Critical Decay Times τ_c for Boundary Relaxation

a_{cor}	Leap-Frog	Euler
>0	$2\Delta t \cdot \left[1 + \sqrt{1 + (2a_{cor} - 1)(2\Delta tf)^2}\right]^{-1}$	$\Delta t \cdot \left[1 + \sqrt{1 + (2a_{cor} - 1)(\Delta tf)^2}\right]^{-1}$
$=0$	$\Delta t \cdot [1 - \Delta tf]^{-1}$	$\Delta t \cdot \left[1 + \sqrt{1 - (\Delta tf)^2}\right]^{-1}$

the IFF meandering is a convective instability in the west followed by an absolute instability in the interior. That is to say, (1) the flow is unstable in the western region; (2) the instability is convective (not absolute). These two statements yield a strong constraint (21) and a weak constraint (22) for d_s, which are rewritten here for easy reference:

$$\frac{2}{\sqrt{-\log(\tau_s R_{abs})}} \leq d_s < \frac{2}{\sqrt{-\log(\tau_s R_{max})}},$$

$$\frac{1}{\sqrt{-\log(\tau_s R_{abs})}} \leq d_s < \frac{m}{\sqrt{-\log(\tau_s R_{max})}}.$$

Here m equals the length scale divided by the horizontal model spacing; it is 4 for a scale of 10 km. For $\tau_s = 12{,}000$ s, and the typical horizontal viscosity $K = 300$ m/s^2, the former yields a d_s around 0.82, and the latter determines its range of variation: (0.41, 1.66). These turn out to be rather accurate results. By sensitivity studies, they are, approximately, 0.8 and (0.5, 1.5). Through the instability analysis it is also found that the model is not sensitive to change in vertical mixing, and horizontal dissipation/diffusion for the momentum and tracer equations. But too much dissipation on the barotropic vorticity equation will result in a premature absolute instability in the western region, and hence a meander intrusion way more upstream the front. Different from dissipation, boundary and temporal relaxations are purely engineering parameters; they must be reassessed once the model setting is changed. But given a basic profile $(\overline{u}, \overline{\rho})$, and a horizontal viscosity K, they can be easily identified by the above constraints.

[59] The forecast was conducted in an operational mode using the Harvard Ocean Prediction System (HOPS) on a hybrid coordinate frame. Prognostic fields were sequentially updated by data acquired on board R/V *Alliance*, whenever available, with a two-scale data assimilation strategy. The events reproduced during the experimental period (14–23 August 1993) include the straightening of the curved frontal axis on 19 August, and the formation of a hammer-head meandering intrusion as mentioned above. They are validated, both qualitatively and quantitatively with those observed from the zigzag survey (18–20 August) and the validation survey (20–23 August). The forecast skill score is high, as evaluated against persistence, in terms of anomaly correlation coefficient and root-mean-square error.

[60] The belief that taking in more data will improve the forecast need not always be true. In the IFF case, if the parameters are set so as to have the convective and/or absolute instabilities precluded or not occurred in order, assimilation of the zigzag data does not help. But, on the other hand, if the model setting admits these processes with appropriate timing and order of occurrence, the information extracted from the zigzag survey does increase the predictability and hence the forecast skill. From a dynamical point of view, the forecast without taking in the zigzag data has reproduced the whole scenario of the baroclinic instability, which appears first in the form of a convective instability, then switched to an absolute instability. The deficiency is that the convective instability is delayed, and both the convective instability and the absolute instability are too weak to yield a meandering intrusion strong enough as observed. The success of the forecast with the zigzag data implies that the assimilation has advanced the convective instability, and has enhanced it both in strength and influence regime. The absolute instability that follows is also greatly enhanced.

[61] The zigzag data assimilation raises a severe issue about the accuracy in field updating: in the presence of spatial error inhomogeneity, large-scale prediction-observation discrepancy may introduce a spurious structure into the posterior fields. (In the present study, this structure may give rise to a spurious buoyancy flow as large as 60 cm/s.) This issue is deeply rooted in the physical processes themselves. In a system with multiscale processes involved, the error field, if not manipulated correctly, may be transferred as an eddy energy across the scale window, leading to a spurious large-scale structure. Clearly, the problem essentially cannot be alleviated just by sophisticating the classical optimization scheme. We need to control over the dynamical as well as the statistical mismatch between the numerical prediction and the observation. In this study, it is fortunate that the large-scale distributions are similar in structure, with roughly a constant in difference; as a result the problem can be fixed using a two-scale window decomposition. In general, a formalism with multiscale consideration may be needed.

[62] From our previous experience with parameter tuning, it is natural to hypothesize that the same rule of thumb must also be obeyed when taking in new data. That is to say, data assimilation must not hurt the fundamental dynamical process(es) underlying the target phenomenon. This should form a constraint in designing an assimilation scheme, which, in a traditional sense, only optimizes the error of the numerics. It is not uncommon that, after updating with new data, the path in the phase space of the corresponding dynamical system is changed. How to have the path kept on the right track, i.e., a dynamically consistent track, after the fields are updated with new data, should be taken into consideration in forming the objective functional. We are therefore working on this kind of data assimilation scheme.

[63] All in all, we have shown through an example that dynamical consistency is of top priority in ocean modeling and simulation. In the case of a highly variable frontal intrusion, namely, the IFF meandering intrusion, the model must be set such that the underlying baroclinic instability, first in the form of a convective instability then an absolute instability, is not hurt or altered, in order to have the hammer-head or deep-sock intrusion recovered. The parameters (especially boundary relaxation, which takes effect jointly with eddy viscosity), must be chosen to admit convective instability, not absolute instability, at the western boundary. If the model setup violates the rule, generally the forecast cannot be successful, even with extra observational data coming in. Here the moral is: in an era when we lay too much stress on numerical modeling and simulation, fundamental geophysical fluid dynamics studies are still of great importance.

Appendix A: Boundary Relaxation

[64] In the HOPS, boundary relaxation is a nudging approach to stabilize the numerical scheme. The following note is based on some material by Patrick Haley, Jr.

(maintained together with the HOPS documentation; see *Haley* [1995]), and private communications from him.

[65] For a prognostic variable u (velocity or tracer), boundary relaxation adds a sponge layer to the near-boundary points. It appears on the right-hand side of the prognostic equation as a Newtonian damping term

$$-\frac{1}{\tau_s}e^{-\left(\frac{d}{d_s}\right)^2}(u-u_0),$$

where d is the distance to the nearest boundary, τ_s and d_s the temporal and spatial decay scales, respectively. This forcing alone gives an exponential decay of u to u_0

$$u = u_0 + Ce^{-\alpha t},$$

where

$$\alpha = \frac{1}{\tau_s}e^{-\left(\frac{d}{d_s}\right)^2}$$

and C is a constant.

[66] The temporal scale τ_s must be set above some critical value, τ_c, in order for the integration to be stable. For a simple system with both nudging and rotation,

$$\frac{du}{dt} - fv + \frac{1}{\tau_s}u = 0$$

$$\frac{dv}{dt} + fu + \frac{1}{\tau_s}v = 0$$

this τ_c can be found analytically using the von Neumann analysis. In general, it is a function of differencing scheme, implicit Coriolis weighting factor a_{cor}, Coriolis parameter f, and time step Δt. (If $a_{cor}=0$, the Coriolis term is treated explicitly; If $a_{cor}=1$, a fully implicit scheme is used. The treatment lies in between when $0 < a_{cor} < 1$.) Table 6 tabulates four expressions for τ_c's with different parameters. In this study, the model uses $a_{cor}=0.5$, $\Delta t = 180s$, $f \approx 1.318 \times 10^{-4}$, and adopts a leap-frog scheme, yielding a critical value $\tau_s = 180$ s.

Appendix B: Spurious Structure Resulting From Data Assimilation in the Presence of Nonuniform Error Distribution

[67] Data assimilation may lead to spurious field structures if the error is not homogeneously distributed. We illustrate this with a highly coarse-grained model, where the physical space is represented by only two points, point 1 and point 2. Suppose there is an observation T_o and a prediction T_p^- for some field T (not necessarily temperature, but any prognostic variable). (Here the superscript "$-$" and "$+$"are used, respective, to signify a field before and after assimilation.) They are evaluated at locations 1 and 2 as $T_o(1)$, $T_o(2)$, $T_p^-(1)$, $T_p^-(2)$, respectively. Suppose further that

$$T_o(1) = T_p^-(1) + C,$$
$$T_o(2) = T_p^-(2) + C,$$

where C is a constant. Then the observed and the predicted fields share an identical spatial *structure*, though the absolute values are not equal. For many fields, one anticipates a correct structure more than the absolute value. Examples in geophysical fluid dynamics include temperature, salinity, density, to name but a few. As the observed and predicted fields have the same structure, ideally we expect the field after assimilation, denoted as $T^+(1)$ and $T^+(2)$, also preserves the structure. However, with the classical OI scheme, this is not possible in general. We now show why.

[68] By optimal interpolation, when no correlation between the observation and model prediction is considered, the assimilated field is

$$T_p^+(1) = \frac{E_o^{-1}(1)T_o(1) + E_p^{-1}(1)T_p^-(1)}{E_o^{-1}(1) + E_p^{-1}(1)},$$
$$T_p^+(2) = \frac{E_o^{-1}(2)T_o(2) + E_p^{-1}(2)T_p^-(2)}{E_o^{-1}(2) + E_p^{-1}(2)},$$

where E_o and E_p are the variance for T_o and T_p, respectively. The new structure, which is characterized by the difference between $T_p^+(2)$ and $T_p^+(1)$, is hence

$$\begin{aligned} T_p^+(2) \quad -T_p^+(1) &= \left[T_p^-(2) - T_p^-(1)\right] + \\ &+ \frac{E_o^{-1}(2)T_o(2) + E_p^{-1}(2)T_p^-(2)}{E_o^{-1}(2) + E_p^{-1}(2)} - \\ &- \frac{E_o^{-1}(1)T_o(1) + E_p^{-1}(1)T_p^-(1)}{E_o^{-1}(1) + E_p^{-1}(1)} \\ &= \left[T_p^-(2) - T_p^-(1)\right] + C \cdot \left[\frac{1}{1+\lambda(2)} - \frac{1}{1+\lambda(1)}\right], \end{aligned}$$

where $\lambda(i) = \frac{E_o(i)}{E_p(i)}$ is the ratio of the observation error to the prediction error at point i ($i = 1,2$). Clearly the posterior difference will not be equal to the priori $\left|T_p^-(2) - T_p^-(1)\right|$, unless $C=0$, or $\lambda(2)=\lambda(1)$. Unfortunately, neither of these conditions are generally satisfied in real problems. That is to say, with the classical OI, assimilation of an observation with the same structure but not identical in values could result in something with a completely different pattern just because of the presence of error nonuniformity.

[69] **Acknowledgments.** The authors are grateful to Arthur J. Miller and Kenneth Brink for important and interesting scientific discussions in the early stage of the preparation of this manuscript. X.S.L. thanks Patrick Haley and Wayne Leslie for their generous help with the HOPS programs and the IFF data set. The explanation of the IFF data by Pierre Lermusiaux, Hernan Arango, and Carlos Lozano are sincerely appreciated. This paper evolved from a previous manuscript (which became sections 4, 5, and 6 here) with Allan R. Robinson (1932–2009), the late Gordon McKay Professor at Harvard University, who does not have the chance to read the rest material any longer; thanks are due to James McCarthy for his sponsorship with the computing facility after ARR passed away. The comments from an anonymous referee helped improve the presentations. This work was partially supported by the Office of Naval Research under Contract N00014-02-1–0989 to Harvard University, by Jiangsu Provincial Government through the "Jiangsu Specially-Appointed Professor Program" (Jiangsu Chair Professorship) to X.S.L., and by the National Science Foundation of China under grant 41276032 to NUIST.

References

Allen, J. T., D. A. Smeed, and A. L. Chadwick (1994), Eddies and mixing at the Iceland-Faeroes Front, *Deep Sea Res., Part I*, *41*(1), 51–79.

Arakawa, A., and V. R. Lamb (1977), Computational design of the basic dynamical processes of the UCLA general circulation model, *Methods Comput. Phys.*, *17*, 174–265.

Astporsson, O. S., A. Gislason, and S. Jonsson (2007), Climate variability and the Icelandic marine ecosystem, *Deep Sea Res., Part II*, *54*, 2456–2477.

Briggs, R. J. (1964), *Electron-Stream Interaction with Plasmas*, MIT Press, Cambridge, Mass.

DelSole, T. (1997), Absolute instability induced by dissipation, *J. Atmos. Sci.*, *54*(21), 2586–2595.

Fox, A. D., and S. J. Maskell (1996), A nested primitive equation model of the Iceland-Faeroe front, *J. Geophys. Res.*, *101*, 18,259–18,278.

Gould, W. J., J. F. Read, and J. Smithers (1987), SEASOAR profiles in the Iceland-Scotland area, May 1987, Rep. 253, 50 pp., Inst. of Oceanogr. Sci., Wormley, U. K.

Griffiths, C. (1995), A fine resolution numerical model of the Iceland-Faeroe front with open boundary conditions, *J. Geophys. Res.*, *100*, 15,915–15,913.

Hansen, B., and J. Meincke (1979), Eddies and meanders in the Iceland-Faroe Ridge area, *Deep Sea Res., Part A*, *26*, 1067–1082.

Haley, P. J., Jr. (1995). *GRIDS User's Guide (Ver. 3.2) HOPS Documentation*, Harvard Univ. Ocean Group, Cambridge, Mass.

Hansen, B., and S. Osterhusb (2000), North Atlantic-Nordic Seas exchanges, *Prog. Oceanogr.*, *45*(2), 109–208.

Held, I. M., R. T. Pierrehumbert, and R. L. Panetta (1986), Dissipative destablization of external Rossby waves, *J. Atmos. Sci.*, *43*, 388–396.

Hopkins, T. S. (1991), The GIN Sea—A synthesis of its physical oceanography and literature review 1972–1985, *Earth Sci. Rev.*, *30*, 175–318.

Huerre, P., and P. Monkewitz (1990), Local and global instabilities in spatially developing flows, *Annu. Rev. Fluid Mech.*, *22*, 473–537.

Kostianoy, A. G., J. C. J. Nihoul, and V. B. Rodionov (2004), *Physical Oceanography of Frontal Zones in the Subarctic Seas, Elsevier Oceanogr. Ser*., vol. *71*, Elsevier, Amsterdam.

Lermusiaux, P. F. J. (1997), Error subspace data assimilation methods for ocean field estimation: Theory, validation and applications, PhD thesis, Div. of Eng. and Appl. Sci., Harvard Univ., Cambridge, Mass.

Lermusiaux, P. F. J. (1999), Estimating and study of mesoscale variability in the Strait of Sicily, *Dyn. Atmos. Oceans*, *29*, 255–303.

Liang, X. S., and A. R. Robinson (2004), A study of the Iceland-Faeroe frontal variability using the multiscale energy and vorticity analysis, *J. Phys. Oceanogr.*, *34*, 2571–2591.

Liang, X. S., and A. R. Robinson (2005), Localized multiscale energy and vorticity analysis. I: Fundamentals, *Dyn. Atmos. Oceans*, *28*, 195–230.

Liang, X. S., and D. G. M. Anderson (2007), Multiscale window transform, *SIAM J. Multiscale Model. Simul.*, *6*(2), 437–467.

Liang, X. S., and A. R. Robinson (2007), Localized multiscale energy and vorticity analysis. II: Theory of finite-amplitude hydrodynamic instability, *Dyn. Atmos. Oceans*, *44*, 51–76.

Liang, X. S., and A. R. Robinson (2009), Multiscale processes and nonlinear dynamics of the circulation and upwelling events off Monterey Bay, *J. Phys. Oceanogr.*, *39*, 290–313.

Lozano, C. J., P. J. Haley, Jr., H. G. Arango, N. Q. Sloan, and A. R. Robinson (1994), Harvard coastal/deep water primitive equation model, in *Reports in Meteorology and Oceanography: Harvard Open Ocean Model Reports*, 15 pp., Div. of Eng. and Appl. Sci., Pierce Hall, Harvard Univ., Cambridge, Mass.

Lozano, C. J., P. Haley Jr., H. Arango, Q. Sloan, and A. R. Robinson (1996), An interdiciplinary ocean prediction system: Assimilation strategies and structured data models, in *Reports in Meteorology and Oceanography: Harvard Open Ocean Model Reports*, Div. of Appl. Sci., Harvard Univ., Cambridge, Mass.

Meincke, J. (1978), On the distribution of low salinity intermediate waters around the Faeroes, *Dtsch. Hydrogr. Z.*, *31*, 50–65.

Miller, A. J., and B. D. Cornuelle (1999), Forecasts from fits of frontal fluctuations, *Dyn. Atmos. Oceans*, *10*, 185–219.

Miller, A. J., et al. (1995a), Quasigeostrophic forecasting and physical processes of Iceland-Faeroe Frontal variability, *J. Phys. Oceanogr.*, *25*, 1273–1295.

Miller, A. J., P.-M. Poulain, A. R. Robinson, H. G. Arango, W. G. Leslie, and A. Warn-Varnas (1995b), Quantitative skill of quasi-geostrophic forecasts of a baroclinically unstable Iceland-Faroe front, *J. Geophys. Res.*, *100*, 10,833–10,849.

Miller, A. J., P. F. J. Lermusiaux, and P.-M. Poulain (1996), A topographic-Rossby mode resonance over the Iceland-Faeroe Ridge, *J. Phys. Oceanogr.*, *26*(12), 2735–2747.

Millero, F. J. et al. (1980), A new high-pressure equation of state of seawater, *Deep Sea Res., Part A*, *27*, 255–264.

Müller, T. J., J. Meincke, and G. A. Becker (1979), The distribution of water masses on the Greenland-Scotland Ridge in August/September 1973, *Ber. Inst. Meereskde*, *62*, 1–172.

Niiler, P. P., S. Piacsek, L. Neuberg, and A. Warn-Varnas (1992), Sea surface temperature variability of the Iceland-Faeroe Front, *J. Geophys. Res.*, *97*, 17,777–17,785.

Peloquin, R. A. (1992), The navy ocean modeling and prediction program, *Oceanography*, *5*, 4–8.

Pistek, P., and D. R. Johnson (1992), A study of the Iceland-Faeroe front using GEOSAT altimetry and current-following drifters, *Deep Sea Res., Part A*, *39*, 2029–2051.

Read, J. F., and R. T. Pollad (1992), Water masses in the Region of the Iceland-Faeroes Front, *J. Phys. Oceanogr.*, *22*, 1365–1378.

Robinson, A. R., H. G. Arango, A. J. Miller, A. Warn-Varnas, P.-M. Poulain, and W. G. Leslie (1996), Real-time operational forecasting on shipboard of the Iceland-Faeroe Frontal variability, *Bull. Am. Meterol. Soc.*, *77*, 243–259.

Scott, J. C., and N. M. Lane (1990), Frontal boundaries and eddies on the Iceland-Faeroes Ridge, in *Ocean Variability and Acoustic Propagation*, edited by J. Potter and A. Warn-Varnas, pp. 449–461, Kluwer Acad.

Shapiro, R. (1971), The use of linear filtering as a parameterization of atmospheric diffusion, *J. Atmos. Sci.*, *28*, 523–531.

Sloan, N. Q. (1996), Dynamics of a shelf-slope front: Process studies and data-driven simulations, PhD thesis, Div. of Appl. Sci., Harvard Univ., Cambridge, Mass.

Smart, J. H. (1984), Spatial variability of major frontal systems in the North Atlantic-Norwegian Sea area: 1980–81, *J. Phys. Oceanogr.*, *14*, 185–192.

Willebrand, J., and J. Meincke (1980), Statistical analysis of fluctuations in the Iceland-Scotland frontal zone, *Deep Sea Res., Part A*, *27*, 1047–1066.